

Deformation and mutual influence of two cylindrical water columns in tandem subjected to shock wave

Zhen-Yu Hong(洪振宇), Yang Song(宋洋), Rui Wang(王睿), Zong-Qiang Ma(马宗强), Dong-Jun Ma(马东军), and Pei Wang (王裴)

Citation: Chin. Phys. B, 2024, 33 (**8**): 084702. DOI: 10.1088/1674-1056/ad5273

What follows is a list of articles you may be interested in

On the spreading behavior of a droplet on a circular cylinder using the lattice Boltzmann method

Fan Yang(杨帆), Hu Jin(金虎), and Mengyao Dai(戴梦瑶)
Chin. Phys. B, 2024, 33 (**6**): 064702. DOI: 10.1088/1674-1056/ad3b7f

Morphological analysis for thermodynamics of cavitation collapse near fractal solid wall

Minglei Shan(单鸣雷), Yu Yang(杨雨), Xuefen Kan(阚雪芬), Cheng Yin(殷澄), and Qingbang Han(韩庆邦)
Chin. Phys. B, 2024, 33 (**6**): 064701. DOI: 10.1088/1674-1056/ad3343

Lattice Boltzmann model for interface capturing of multiphase flows based on Allen-Cahn equation

He Wang(王贺), Fang-Bao Tian(田方宝), and Xiang-Dong Liu(刘向东)
Chin. Phys. B, 2022, 31 (**2**): 024701. DOI: 10.1088/1674-1056/ac11d8

A mass-conserved multiphase lattice Boltzmann method based on high-order difference

Zhang-Rong Qin(覃章荣), Yan-Yan Chen(陈燕雁), Feng-Ru Ling(凌风如), Ling-Juan Meng(孟令娟), Chao-Ying Zhang(张超英)
Chin. Phys. B, 2020, 29 (**3**): 034701. DOI: 10.1088/1674-1056/ab6834

Gradient-augmented hybrid interface capturing method for incompressible two-phase flow

Zheng Fu(付峥), Shi-Yu Wu(吴士玉), Kai-Xin Liu(刘凯欣)
Chin. Phys. B, 2016, 25 (**6**): 064701. DOI: 10.1088/1674-1056/25/6/064701

Deformation and mutual influence of two cylindrical water columns in tandem subjected to shock wave

Zhen-Yu Hong(洪振宇)[1,2], Yang Song(宋洋)[1], Rui Wang(王睿)[1], Zong-Qiang Ma(马宗强)[1], Dong-Jun Ma(马东军)[1,†], and Pei Wang (王裴)[1,3]

[1] *Institute of Applied Physics and Computational Mathematics, Beijing* 100094, *China*
[2] *Graduate School of China Academy of Engineering Physics, Beijing* 100088, *China*
[3] *Center for Applied Physics and Technology, Peking University, Beijing* 100871, *China*

(Received 18 March 2024; revised manuscript received 10 May 2024; accepted manuscript online 31 May 2024)

The interaction between shock waves and multiple cylinders, referred to as shock–cylinder interaction (SCI), is an important phenomenon in science and engineering. However, its underlying physical mechanisms remain unclear. This study entailed the numerical simulation of the aerobreakup of two tandem water columns subjected to a high-speed gas flow by using an adaptive mesh refinement (AMR)-based diffusion-interface model. The objective was to elucidate the changes in water–column deformation patterns over a wide range of Weber numbers. Statistical analysis was performed to examine the deformation of the water columns in vertical directions. Results reveal distinct deformation patterns between the two columns as the Weber number increases. Additionally, an extended exponential stretching law model was devised, and its improved capability to predict the deformation patterns was demonstrated.

Keywords: shock–cylinder interaction (SCI), Weber number effect, aerobreakup, multiphase flow

PACS: 47.40.–x, 47.55.df, 47.61.Jd **DOI:** 10.1088/1674-1056/ad5273

1. Introduction

The interaction between shock waves and water droplets is a ubiquitous phenomenon in natural high-speed flows and has garnered considerable interest in engineering research.[1] Specifically, detached shock waves can interact with rain droplets, leading to the erosion of aircraft surfaces.[2] Fuel droplets interact with shock waves in aircraft engines, and their particle-size distribution plays a crucial role in the efficiency of atomization and combustion, ultimately affecting engine performance.[3] This complex process also entails the generation of intricate instabilities. Given the scientific and engineering implications of droplet–shock wave interaction, research progress in this area is crucial.

Extensive experimental and theoretical research has been focused on the interplay between shock waves and droplets. In 1950s, Hinze conducted a pioneering theoretical study on the deformation and fragmentation of individual droplets exposed to high-speed gas flow. The Weber number, *i.e.*, the ratio between the aerodynamic inertia of the gas flow and the surface tension effect of the droplets, was employed as a key parameter to delineate various modes of droplet fragmentation.[3] Notably, an increase in the Weber number corresponds to the manifestation of different droplet breakup modes. Subsequently, Pilch and Erdman[4] and Guildenbecher *et al.*[5] refined the classification of droplet breakup modes, categorizing them based on their distinct morphologies, namely, vibrational breakup, bag breakup, bag-and-stamen breakup, shear breakup, and catastrophic breakup.

Owing to experimental limitations, achieving an accurately characterization of the spatial and temporal characteristics of droplet morphology is challenging, especially when investigating the shear fragmentation of droplets at high Mach and Weber numbers. In these scenarios, small interfacial wave scales and interference from water mist disrupt experimental observations. Consequently, measuring the interfacial evolution and internal flow fields of the droplet becomes remarkably difficult. Recently, researchers have employed various numerical methods to simulate the aerodynamic fragmentation of isolated droplets in both two dimensions and three dimensions.[6–10] Their findings indicate that instability development at the interface and non-uniform pressure distribution around the droplet significantly influence the fragmentation process. The evolution characteristics of waves inside a droplet also remains a topic that has attracted the attention of many researchers. Wang *et al.* developed a 5th-order WENO method[11] to study the evolution of low-pressure regions inside droplets after their collision with shock waves[12] and the fluctuating structure inside the shocked water column.[13] It is found that the first and second reflected waves focus inside the water column regardless ofwhether the shape of the incident shock wave is convergent, planar or divergent.

Building upon both experimental observations and numerical simulation results, various researchers have proposed theoretical models to elucidate the primary physical mechanisms governing the droplet fragmentation process.[14,15] Theofanous and Li[16] employed laser-induced fluorescence (LIF) to investigate the aerodynamic breakup of droplets at high We-

†Corresponding author. E-mail: ma_dongjun@iapcm.ac.cn

© 2024 Chinese Physical Society and IOP Publishing Ltd

ber numbers, and their findings indicate that droplet breakup is predominantly governed by two mechanisms: Rayleigh–Taylor (RT) piercing and shear-induced entrainment. The RT instability and surface tension dominate the former mechanism, leading to droplet breakup for Weber numbers within the range of $10 < We < 100$. However, the latter mechanism is characterized by Kelvin–Helmholtz instability and shear-induced entrainment, resulting in droplet breakup for Weber numbers exceeding 1000. When Weber numbers fall within the range of 100–1000, these two mechanisms compete with each other.

In practical scenarios, the flow field usually involves numerous mutually interacting droplets. For instance, the interaction of shock waves with multiple droplets/cylinders is prevalent in aircraft engines and implosion situations. Consequently, extensive research efforts have sought to address this complex problem. Several experimental studies have focused on changes in the drag coefficient under low Weber numbers and low Reynolds numbers for both monodisperse flow of droplets[17–20] and interactions involving multiple droplets.[21,22] These studies have revealed a reduction in the drag coefficient of downstream droplets compared to those upstream. Furthermore, numerous numerical investigations have been performed on the deformation and breakup of droplets/columns in tandem.[23–29] An illustrative example is the study by Stefanitsis *et al.*,[28] wherein the aerodynamic fragmentation behaviors of four droplets placed in tandem in a diesel engine were simulated with Weber numbers ranging from 15 to 64 and dimensionless distances (L/D_0) between droplet centers varying from 1.25 to 20. They subsequently proposed a new fragmentation mode for the deformation of the third droplet. While single-droplet aerodynamic fragmentation studies are prevalent, research on the aerodynamic coupling deformation and fragmentation of multiple droplets is relatively scarce. Investigating the interaction mechanism between multiple droplets/cylinders and its impact on aerodynamic deformation is therefore crucial. Such studies potentially contribute to the development of models that account for interphase interactions in the two-phase flow model of droplet clouds under the influence of high-speed airflows.

Despite numerous studies on the shock–cylinder interaction (SCI) problem, the aerobreakup of multiple droplets/cylinders under varying Weber numbers and the interaction between deformed droplets/cylinders remain unclear. This study aimed to explore the intricate interactions between shock waves and interfaces, focusing on the aerobreakup of two tandem water columns exposed to shock waves spanning a wide range of Weber numbers. Section 2 outlines the numerical method employed in this study, while Section 3 presents a case validation by comparing its results with experimental data and the basic setup of the algorithm. The computational results are detailed in Section 4. Finally, conclusions and discussions are presented in Section 5.

2. Numerical method

The SCI involves a broad range of different temporal and spatial scales, and its numerical simulations are computationally demanding. Aerobreakup is governed by the compressible Navier–Stokes (NS) equations for the liquid and surrounding gas flow, coupled with the continuity and stress equivalence on the deformed surface. Therefore, in order to accurately simulate the fragmentation of the water column, an interface trapping scheme that combines a multi-component flow model with a shock wave trapping finite evolution method is used. This scheme is also referred to as the diffusive interface approach. This is because, although the interface is not sharp and is explicitly tracked, the scheme allows for some numerical diffusion at the interface. This facilitates discrete conservation, consistent thermodynamics in the mixing cell, and dynamic emergence or disappearance of the interface.

Non-mixed-phase fluids in mechanical equilibrium were considered and the model proposed by Kapila *et al.*[30] was used. To guarantee simulation stability, Saurel *et al.*[31] employed a pressure relaxation method to converge from the pressure disequilibrium formulation to its equilibrium. The surface tension was modelled according to Schmidmayer *et al.*[32] to capture its effects.

The viscous pressure-disequilibrium multi-component model considering the two-component surface tension effect is

$$\frac{\partial \alpha_1}{\partial t} + u\cdot\nabla\alpha_1 = \mu\left(p_1 - p_2\right), \tag{1}$$

$$\frac{\partial \alpha_1\rho_1}{\partial t} + \nabla\cdot(\alpha_1\rho_1 u) = 0, \tag{2}$$

$$\frac{\partial \alpha_2\rho_2}{\partial t} + \nabla\cdot(\alpha_2\rho_2 u) = 0, \tag{3}$$

$$\frac{\partial \rho u}{\partial t} + \nabla\cdot(\rho u\otimes u + pI + \Omega - \tau) = 0, \tag{4}$$

$$\begin{aligned}&\frac{\partial \alpha_1\rho_1 e_1}{\partial t} + \nabla\cdot(\alpha_1\rho_1 e_1 u) + \alpha_1 p_1\nabla\cdot u\\ =\ & -\mu p_I\left(p_1 - p_2\right) + \alpha_1\tau_1 : \nabla u,\end{aligned} \tag{5}$$

$$\begin{aligned}&\frac{\partial \alpha_2\rho_2 e_2}{\partial t} + \nabla\cdot(\alpha_2\rho_2 e_2 u) + \alpha_2 p_2\nabla\cdot u\\ =\ & \mu p_I\left(p_1 - p_2\right) + \alpha_2\tau_2 : \nabla u,\end{aligned} \tag{6}$$

$$\frac{\partial f}{\partial t} + u\cdot\nabla f = 0, \tag{7}$$

where α_i, p_i, ρ_i, and e_i are the volume fraction, pressure, density, and internal energy of component i, respectively, and u is the mixing velocity. The mixing density and pressure are given by

$$\rho = \alpha_1\rho_1 + \alpha_2\rho_2, \tag{8}$$

$$p = \alpha_1 p_1 + \alpha_2 p_2. \tag{9}$$

The surface tension tensor is expressed as

$$\Omega = -\sigma\left(\|\nabla f\| I - \frac{\nabla f\otimes\nabla f}{\|\nabla f\|}\right), \tag{10}$$

where σ is the surface tension coefficient, and f is a color function. The viscous stress tensor is expressed as

$$\tau = 2\eta\left(\frac{1}{2}\left(\nabla u + (\nabla u)^{\mathrm{T}}\right) - \frac{1}{3}(\nabla\cdot u)I\right), \tag{11}$$

where η is the mixing shear viscosity coefficient, and τ_i is the viscous stress tensor component of component i. Further, μ is the pressure relaxation coefficient, and the pressure at the interface is

$$p_{\mathrm{I}} = \frac{z_2 p_1 + z_1 p_2}{z_1 + z_2}, \tag{12}$$

where $z_i = \rho_i a_i$ is the acoustic impedance of component i, and a_i is the acoustic velocity of component i.

In this model, for $p_1 \neq p_2$, the total energy equation for the mixture is replaced by the internal energy equation for each component. However, the mixture-total energy equation for the system can be written in the usual form as

$$\frac{\partial \rho E}{\partial t} + \nabla\cdot\left((\rho E + p + \varepsilon_\sigma)u + \Omega\cdot u - \tau\cdot u\right) = 0, \tag{13}$$

where the total energy is

$$E = e + \frac{1}{2}\|u\|^2, \tag{14}$$

the internal energy is

$$e = \sum_{i=1}^{2} Y_i e_i(\rho_i, p_i), \tag{15}$$

and the capillary energy is

$$\varepsilon_\sigma = \sigma\|\nabla f\|, \tag{16}$$

where the internal energy component can be calculated from the equation of state. The mass fraction is

$$Y_k = \frac{\alpha_k \rho_k}{\rho}. \tag{17}$$

The ideal gas equation of state can be used for the gas phase to yield

$$p_{\mathrm{g}} = \left(\gamma_{\mathrm{g}} - 1\right)\rho_{\mathrm{g}} e_{\mathrm{g}}. \tag{18}$$

The water phase is approximated by a rigid gas equation of state to approximate the intrinsic relationship as follows:

$$p_{\mathrm{l}} = (\gamma_{\mathrm{l}} - 1)\rho_{\mathrm{l}} e_{\mathrm{l}} - \gamma_{\mathrm{l}} P_\infty. \tag{19}$$

The parameters used in the equation of state are shown in Table 1. The term γ_{l} is based on the study by Le Métayer *et al.*[33] Meanwhile, the terms μ_{l}, P_∞, and σ are as reported by Kaiser *et al.*[34]

Table 1. Physical properties used in the simulation.

	ρ (kg·m^{-3})	p_0 (Pa)	P_∞ (Pa)[b]	γ (−)[a]	μ (Pa·s)[b]	σ (N/m)[b]
Water	1000	101325	3.43×10^8	2.35	1.0×10^{-3}	72.75×10^{-3}
Air	1.204	101325	–	1.4	1.85×10^{-5}	–

[a]Ref. [33], [b]Ref. [34].

The solution of the model occurs in three steps. Initially, the hyperbolic pressure-disequilibrium model is solved, where the governing equations are decoupled from the advection of the color function and surface tension effects. Subsequently, the surface tension model is solved, and finally, the pressure relaxes until an equilibrium state is achieved.

The specific steps in the process as follows:

(i) The pressure disequilibrium model is solved using the Gudonov-type method. At the material interface, the interfacial fluxes are calculated using the Harten–Lax–van Leer contact (HLLC) approximate Riemann solver, wherein the governing equations are decoupled from the advection and surface tension effects of the color function. The scheme is a finite-volume MUSCL-Hancock method[35] with the second-order accuracy in spatial discretization and the first-order accuracy in temporal discretization. In addition, the monotonized central[35] slope limiter is combined with the THINC interface sharpening technique to minimize interface diffusion.[36]

(ii) The hyperbolic surface tension model is solved to ensure conservation of momentum and energy. The surface tension was modelled according to Schmidmayer *et al.*[32] to capture its effects.

(iii) Infinite pressure relaxation ($\mu \to +\infty$) is employed, resulting in the convergence to a thermodynamically consistent mechanical equilibrium model.

$$\boldsymbol{q} = \begin{bmatrix} \alpha_k \\ \alpha_k\rho_k \\ \rho\boldsymbol{u} \\ \alpha_k\rho_k e_k \end{bmatrix}, \tag{20}$$

$$\boldsymbol{r} = \begin{bmatrix} \delta p_k \\ 0 \\ \boldsymbol{0} \\ -p_{\mathrm{I}}\delta p_k \end{bmatrix}, \tag{21}$$

$$\delta p_k = \sum_{j\neq k}^{N} \mu_{k,j}(p_k - p_j). \tag{22}$$

The pressure-disequilibrium model can be solved with an infinite relaxation procedure. At each time step then we solve the system of ordinary differential equations (ODE)

$$\frac{\partial \boldsymbol{q}}{\partial t} = \boldsymbol{r}(\boldsymbol{q}), \tag{23}$$

that relaxes the disequilibrium pressures for $\mu \to +\infty$. In the case of the infinite relaxation (stiff pressure relaxation), $\mu \to +\infty$, the model converges to a single, equilibrium pressure. We use the infinite-relaxation procedure of Saurel *et al.*[31]

In order to save computational resources, Schmidmayer *et al.*[37] developed an adaptive mesh refinement (AMR) technique that is used based on the variation of the volume fraction, density, pressure, and velocity.

This modelling has been implemented in the novel open-source code ECOGEN.[38]

3. Validation and computational model settings

3.1. Validation based on experiment Igra and Takayama

A grid sensitivity study was conducted using three different uniform grids with resolutions of $d/\Delta x = 25$, 50, and 100 to identify the appropriate spatial resolution required to resolve the scales of interest. Figure 1(a) shows the droplet shapes for each grid size. To quantify the results of the grid sensitivity analysis, time evolution of the parent cylinder's area (normalized by the area of undeformed cylinder) is computed for each of the three grid sizes. Figure 1(b) compares the areas obtained from the three cases and show that the results converge for the grids with resolutions of $d/\Delta x = 50$ and 100. Therefore, for this validation study, a grid size of $d/\Delta x = 50$ was chosen. Limited by the available computational resources, we chose the AMR level of 1.

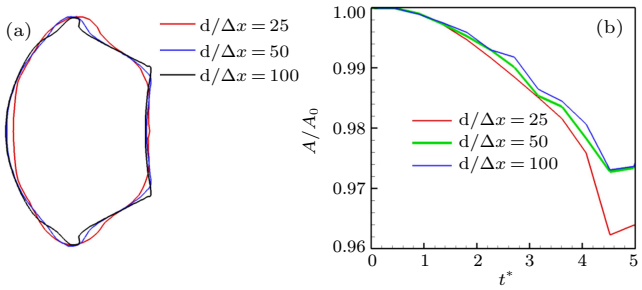


Fig. 1. Grid sensitivity analysis (a) parent cylinder shape for different grid sizes at $t^* = 13.55$; (b) time evolution of parent cylinder area at the three different grid sizes with resolutions of $d/\Delta x = 25$, $d/\Delta x = 50$, and $d/\Delta x = 100$.

A two-dimensional (2D) case was considered to verify the reliability of the program calculations with reference to the parameters of the experiment by Igra and Takayama.[22] In their experiment, two water columns with a diameter of $D_0 = 4.8$ mm and a front-back distance of $l_0 = 30$ mm are placed in the static gas inside the shock tube, and the shock wave Mach number is 1.47. The dimensionless time $t^* = t \cdot u_s/D_0$. To simulate this experiment, we use a rectangular test section of size 129.6 mm $(27D_0)$ by 38.4 mm $(8D_0)$. The cylinder was placed at a distance of 24 mm from the left boundary. The shock wave travels from left to right. The shock wave travels from left to right. The corresponding Reynolds and Weber numbers are 1.12×10^5 and 6900, respectively.[22]

Table 2. Parameters used in the experiment and simulation.

	D_0 (mm)	Mach number	Front-back distance (mm)	$We(\rho_g u_g^2 d_0/\sigma)$	$Re(\rho_g u_g d_0/\mu_g)$	Test section/computational domain (mm×mm)
Experiment[a]	4.8	1.47	30	6900	112000	150×60
Simulation	4.8	1.47	30	6900	112000	129.6×38.4

[a]Ref. [22].

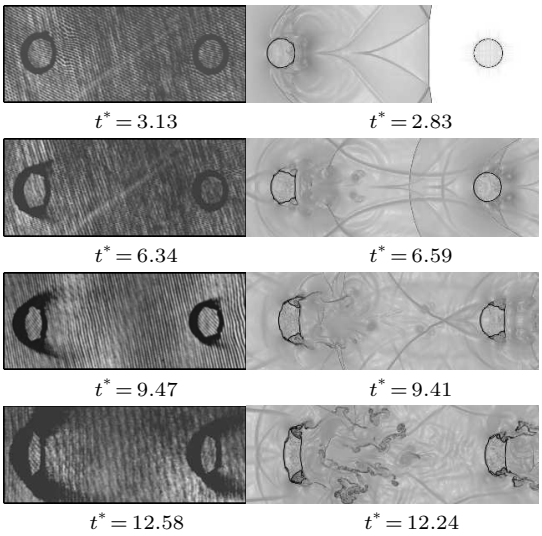


Fig. 2. Comparison between experiment in Ref. [22] (left column) and present simulations (right column) at $t^* = 3.13$, 6.34, 9.47, and 12.58. $t^* = t \cdot u_s/D_0$.

As is shown above, we made sure that the experimental and simulation parameter settings were consistent.

Table 3. Comparison of the deformation between the experiment in Ref. [22] and present results for the upstream cylinder at similar non-dimensional times.

Igra–Takayama experiment[a]		Present simulations		Deviation from experiment
t^*	A/A_0	t^*	A/A_0	%
0.3	0.9548	0.49	0.98799	3.36
2.4	0.9419	2.79	0.94427	0.25
3.45	0.9306	3.45	0.94284	1.3
6.787	0.9242	6.75	0.92881	0.49
9.757	0.91935	9.71	0.90996	1.02
12.788	0.9322	12.68	0.88817	4.72

[a]Ref. [22].

Figure 2 presents a comparison of the flow field between the previously reported experiment and the present simulation results at different non-dimensional time; a good agreement is evident. Based on the qualitative (Fig. 2) and quantitative

(Table 3 and Figs. 3 and 4) comparisons, it can be inferred that our simulations accurately capture the experimentally observed liquid phase behaviors.

Table 3 presents a comparison of the variation of the upstream water column area in the previous experiment and the present simulation results at different non-dimensional time. The deformation is estimated by calculating the area of the liquid phase (normalized by the area of the un-deformed cylinder).

Figure 3(a) illustrates the time evolution of the ratio of the width to the initial diameter of the water column in the direction perpendicular to the shock wave at different moments, whereas figure 3(b) shows the time evolution of the ratio of the width to the initial diameter of the water column in the direction along the shock wave at different moments. La is the maximum width of the water column in the transverse direction, and Lb is the maximum width of the water column in the streamwise direction. As evident from the figure, La continuously increases, and the growth rate is larger when $t^* < 15$. Lb decreases at a constant rate.

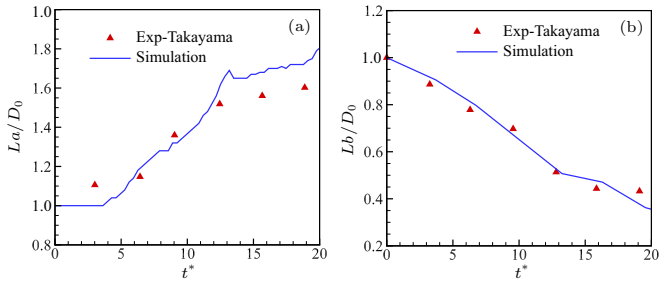


Fig. 3. Comparison of lateral deformation and streamwise deformation between experiment[22] and present results for the upstream column: (a) lateral deformation and (b) streamwise deformation.

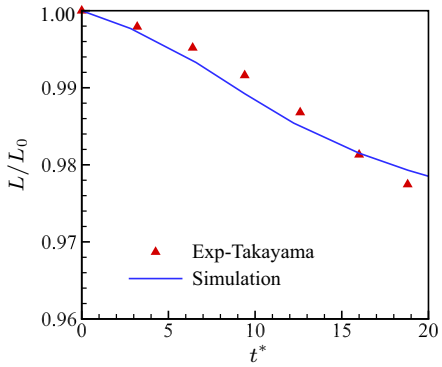


Fig. 4. Time variations of normalized distance between the barycenter of two columns.

Figure 4 shows the normalized distance of the barycenters of two columns, in which L is the distance of the barycenter of two columns. The afore-described qualitative and quantitative statistical results indicated that the simulation results are in good agreement with the experimental results; the reliability of the simulation results was thus validated.

3.2. Computational model settings

In our simulations, we set the shock wave strength $Ma = 1.47$, Reynolds number $Re = u_s D_0/\nu$, and Weber number $We = \rho_g u_s^2 D_0/\sigma$ consistent with the previous experiment mentioned above. Here, D_0, ν, u_s, and σ are the initial droplet diameter, kinematic viscosity coefficient of the gas, post-wave gas velocity, and surface tension coefficient, respectively. We varied the Re and We values by changing the water column diameter and examined the water column deformation fragmentation state corresponding to the values within the range of $We = [18, 367]$.

The simulations were performed in a rectangular computational domain of $[0,\ 19D_0] \times [0,\ 5D_0]$. The choice of the region size is based on a sensitivity study that was performed with the aim of minimizing the influence of the regional boundary conditions and the computational burden. The true direct numerical simulation of the entire flow field and interfacial shock wave interactions under 3D flow conditions is extremely difficult to achieve. Therefore, we simulated the interactions between two columns and the shock wave in two dimensions. Its initial setup is shown in Fig. 5. The two columns are initially at rest, the upstream water column is placed at $(5D_0,\ 2.5D_0)$, the downstream water column is placed at $(9D_0,\ 2.5D_0)$, and the initial position of the shock wave is $x = 4D_0$. The left and right boundaries are ascribed non-reflective boundary conditions, and the top and bottom boundaries follow solid-wall boundary conditions. To ensure high temporal and spatial accuracy without incurring excessive computational costs, the adaptive mesh comprises two layers that are adjusted to shocks, interfaces, and turbulence. The maximum Courant–Friedrichs–Lewy (CFL) number is set to 0.6.

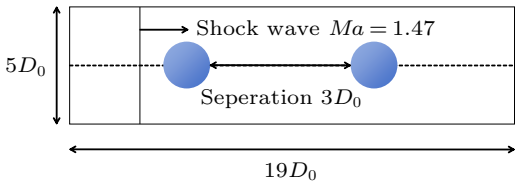


Fig. 5. Schematic diagram of computational domain.

Table 4. Diameters of water column and the corresponding We values.

Initial diameter D_0 (μm)	12	24	48	96	240
$We = \rho_g U^2 D_0/\sigma$	18.3	36.7	73.4	146.8	367.1

In this study, we examined the aerobreakup of two tandem water columns under different We values (as shown in Table 4). The initial distance of the water column center of mass was set to four times that of the initial diameter, and the We value was varied by changing the water column diameter.

4. Results and discussion

The effects of Weber number and diameter on the deformation fragmentation behaviour are systematically illustrated by extracting and describing the evolutionary laws of typical features during droplet evolution.

4.1. Breakup morphology

Figures 6–10 show the distributions of physical quantities of the flow field of the water column at typical instances with different *We* values. In order to represent the material interface, the contours of the water volume fraction $\alpha_l = 0.5$ were extracted.

When $We = 18.3$, neither column experiences breakups. Instead, the upstream column is flattened by the pressure difference between the high-pressure region on the windward side and the low-pressure region between the two columns. This creates a curved windward side and a flat leeward side. In the downstream column, the region of high pressure emerges midway between the two columns, encircling the beginning of the column. Owing to the pressure difference and the airflow's shear effect, the equatorial zone extends outwards. It then evolves into a region of downstream pressure that is superior to that of the upstream one. As a result, the equatorial region of the downstream column stretches and curves further towards the middle than that of the upstream column, eventually adopting a horseshoe-like shape.

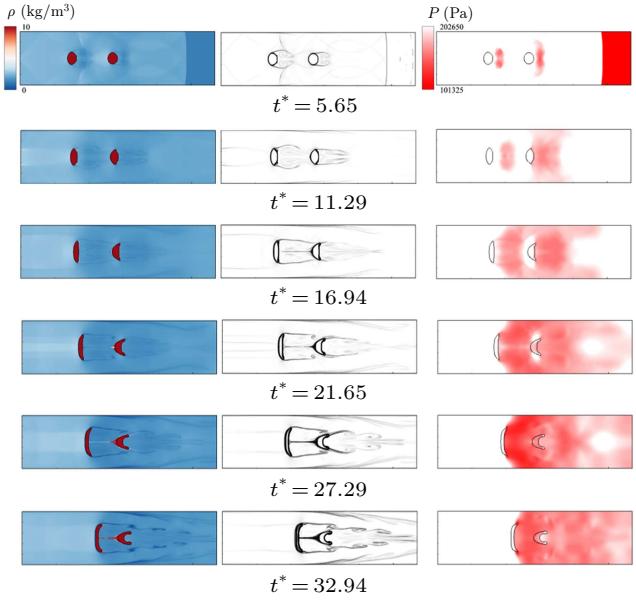


Fig. 6. Contours of density (left column), density gradient (middle column), and pressure (right column) at $t^* = 5.65$, 11.29, 16.94, 21.65, 27.29, and 32.94 for $We = 18.3$, $t^* = t \cdot u_s/D_0$.

When $We = 36.7$, the deformation mode of the upstream column remains the same as in the case of the previous *We* value, and only the flattening becomes more pronounced. However, as regards the downstream column, the deformation mode changes to the bag breakup mode. In this mode, the liquid film stretches out under high pressure in the equatorial region to create a baggy structure, and the windward side is flattened.

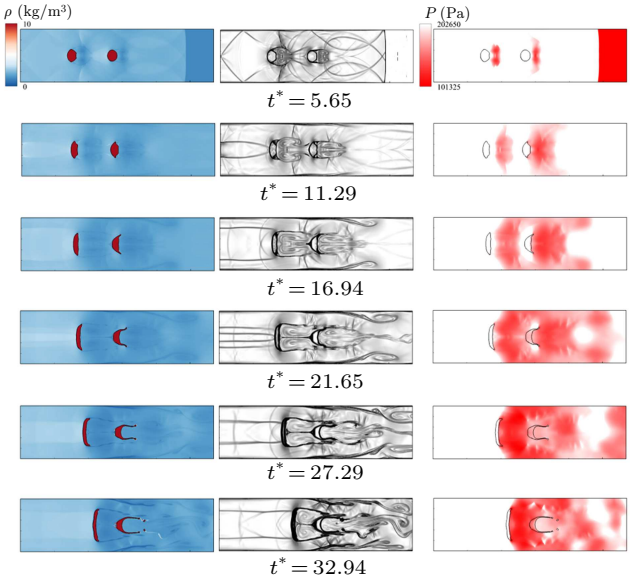


Fig. 7. Contours of density (left column), density gradient (middle column), and pressure (right column) at $t^* = 5.65$, 11.29, 16.94, 21.65, 27.29, and 32.94 for $We = 36.7$, $t^* = t \cdot u_s/D_0$.

When $We = 73.4$, both of the columns undergo bag breakup mode. However, the key distinction is that the upstream column undergoes significant flattening, whereas the windward side of the downstream column retains a platform-like structure. The leeward side is concave towards the upstream direction. Additionally, the equatorial region of the downstream column stretches out into a longer liquid film owing to the shear of the airflow, resulting in a more intricate structure. This structure further breaks down into a liquid band and mist.

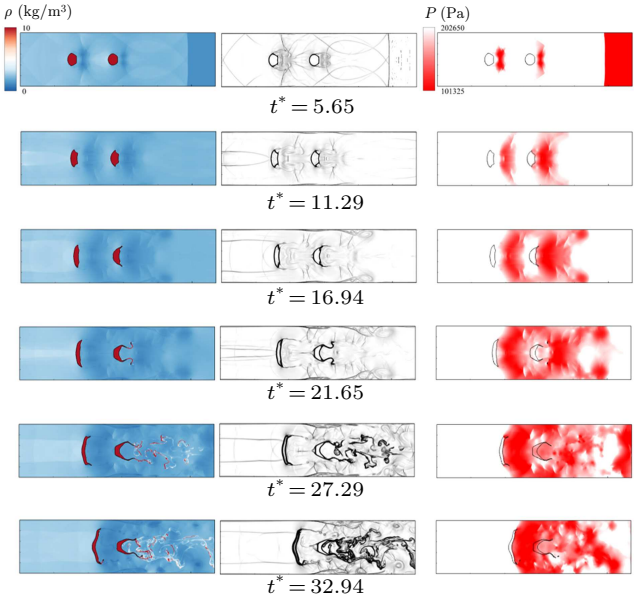


Fig. 8. Contours of density (left column), density gradient (middle column), and pressure (right column) at $t^* = 5.65$, 11.29, 16.94, 21.65, 27.29, and 32.94 for $We = 73.4$, $t^* = t \cdot u_s/D_0$.

When $We = 146.8$, the upstream column shifts to the shear stripping mode, while the downstream column adopts

a bag-and-stamen breakup mode. The film of liquid that extends into the equatorial area of the upstream column is separated by the shear, eventually forming a structure resembling a bag. In contrast, the front-facing surface of the downstream column maintains a flattened surface at the initial stage, while the rear-facing surface of the upstream column remains level. Subsequently, the platform vanishes, and the wind-facing surface develops into a structure that resembles fingers or stamens. Simultaneously, the concave leeward surface of the upstream column bends forward, while the leeward side of the downstream column continues to stretch and form a bag-like shape before separating.

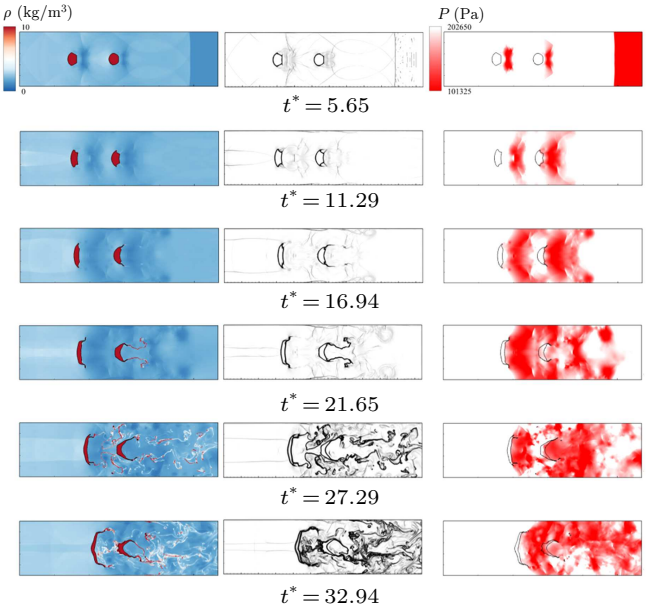


Fig. 9. Contours of density (left column), density gradient (middle column), and pressure (right column) at $t^* = 5.65$, 11.29, 16.94, 21.65, 27.29, and 32.94 for $We = 146.8$, $t^* = t \cdot u_s/D_0$.

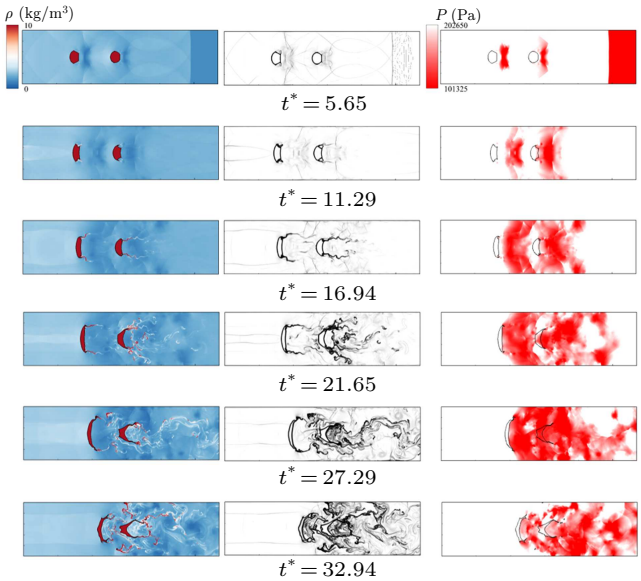


Fig. 10. Contours of density (left column), density gradient (middle column), and pressure (right column) at $t^* = 5.65$, 11.29, 16.94, 21.65, 27.29, and 32.94 for $We = 367.1$, $t^* = t \cdot u_s/D_0$.

When $We = 367.1$, the upstream column remains in shear stripping mode. However, the liquid film around the equator starts to stretch away from the cylinder body before flattening further, resulting in the advancement of the dimensionless time of liquid film detachment. The downstream column maintains the bag-and-stamen breakup mode but with the flattening destabilization of the windward side advancing compared to the previous scenario, resulting in the earlier appearance of the stamen-like structure.

Figure 11 shows the distribution of vorticity in the flow field under different *We* values. The vorticity is symmetrically distributed; two vortex structures would be formed on the leeward side of two water columns, and under the effect of vortex convolution, the material on the surface of the downstream water columns would be sheared and entrained out to form a jet-like structure.

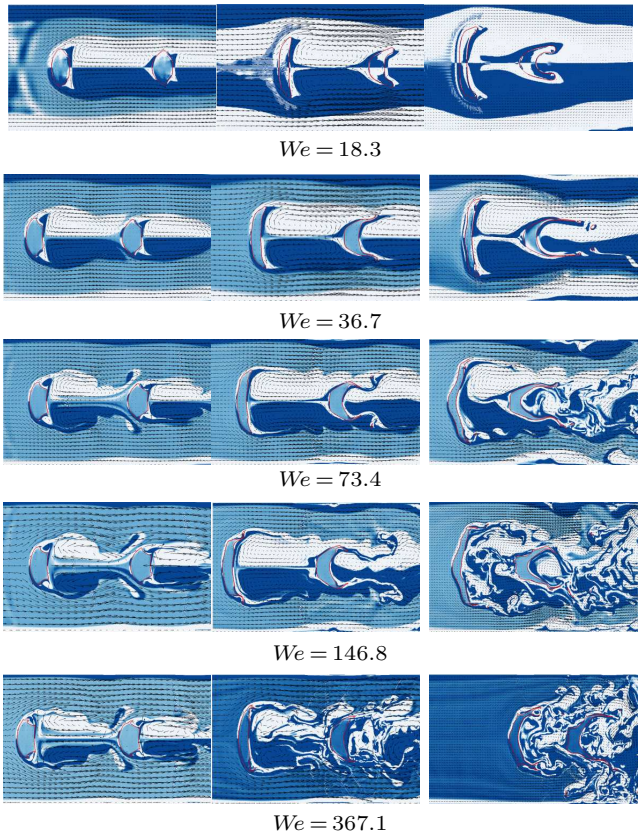


Fig. 11. Contours of vorticity at $t^* = 11.29$ (left column), 21.65 (middle column), and 32.94 (right column) for different *We* values. $t^* = t \cdot u_s/D_0$.

4.2. Motion and deformation of water columns

Additional data on the motions and deformations of the two columns in the simulation results were computed. This includes their displacements, distance, velocity, acceleration, and the maximum width of the transverse deformations over time. These calculations aid the analysis of the movements of both columns and their influence on each other's movements and deformations under varying *We* values.

Figure 12(a) shows the dimensionless displacements x/D_0 of the two columns corresponding to different *We* values.

All upstream columns have similar displacements in different conditions, and the displacements of the upstream columns are three times as much as the displacements of the downstream columns owing to the larger acceleration of the upstream water columns. Figure 12(b) shows the dimensionless distance between two water columns at different *We* values over time, and the distance between two water columns decreases gradually owing to the larger displacement of the upstream water column. This is generally consistent with the variation of the dimensionless distance of water columns under different *We* values.

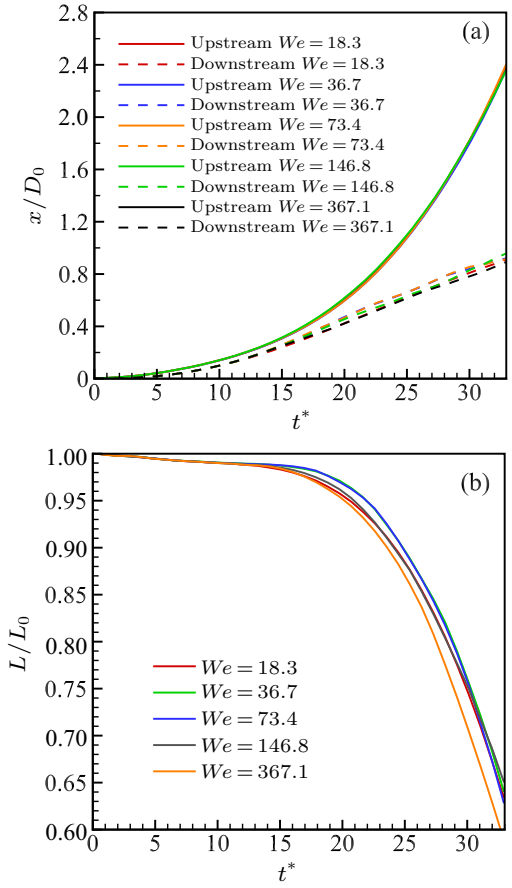


Fig. 12. Time variations of (a) streamwise translation for two columns and (b) distance between two columns corresponding to different *We* values. In panel (a), the solid lines represent the upstream column, and the dotted lines represent the downstream column.

Figure 13(a) shows the upstream water column velocity corresponding to different *We* values. Evidently, under different conditions, the upstream water column velocity in the same dimensionless time is essentially the same, increasing from 0 to 40–45. Figure 13(b) shows the acceleration of the two columns of the logarithmic coordinates of the curve with time for different *We* values; the acceleration is inversely proportional to the radius.

Figure 14(a) shows the downstream column velocity corresponding to different *We* values. Under different conditions, the water column velocity is essentially the same at the same dimensionless time when $t^* < 15$, and the maximum speed is within 8 m/s–10 m/s, that is, only one quarter of the maximum velocity of the upstream column. Figure 14(b) shows the variation of the two-column acceleration with time corresponding

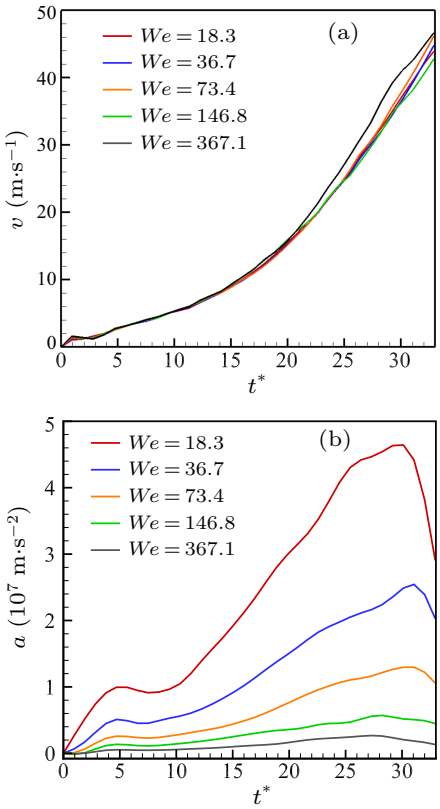


Fig. 13. Time variations of (a) velocity and (b) acceleration for upstream columns corresponding to different *We* values.

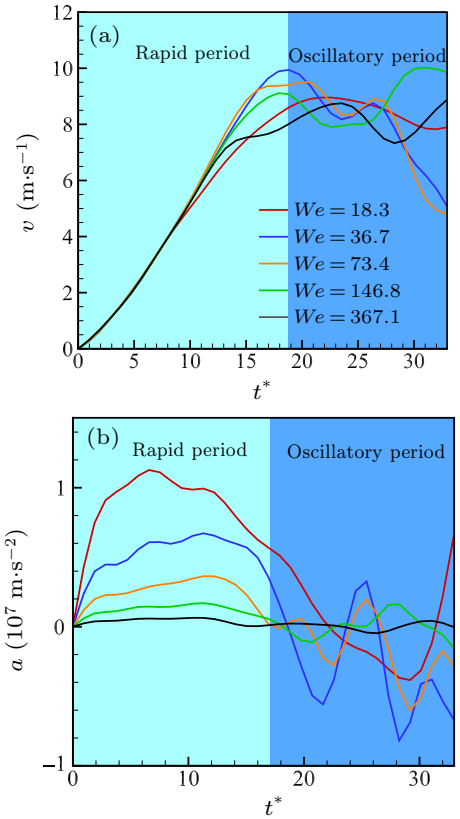


Fig. 14. Time variations of velocity (a) and acceleration (b) for downstream columns corresponding to different *We* values.

to different *We* values. When $t^* < 15$, the acceleration is inversely proportional to the radius; however, fluctuations subsequently become larger, with no evident trend.

Figure 15 shows the transverse deformation of the upstream column. La is the maximum width of the water column in the transverse direction. For low *We*, the transverse deformation in the entire stage evidently increases. At this time, the water column morphology is embodied in the flattening; when *We* continues to increase, because the edge of the water column is gradually being peeled off by the shear, transverse deformation first increases and then decreases.

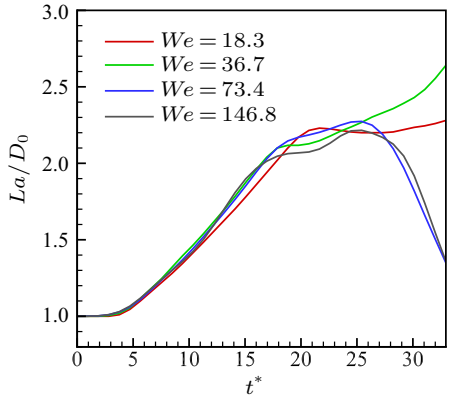


Fig. 15. Time variations of lateral deformation of upstream column for different *We* values.

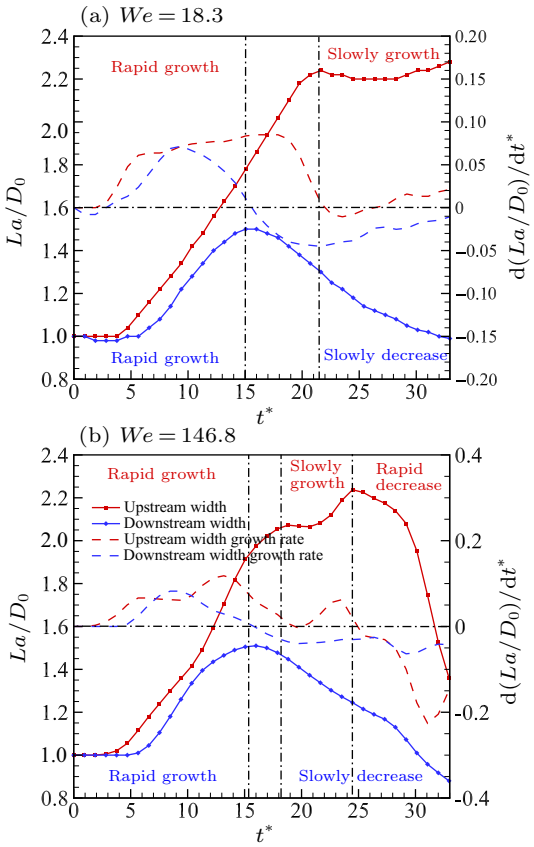


Fig. 16. Time variations of lateral deformation of two columns. The red lines represent the upstream column and the blue lines the downstream column. The solid lines indicate the lateral deformation and the dotted lines indicate the growth of the lateral deformation. (a) $We = 18.3$ and (b) $We = 146.8$.

Figures 16(a) and 16(b) show comparisons of the lateral deformation of the two water columns for different *We* values. Evidently, the maximum width of lateral deformation of the upstream water column is always larger than that of the downstream column, and the ratio of the maximum value of upstream and downstream columns, La/D_0, is maintained at approximately 1.5. When $t^* < 20$, the width of the upstream water column grows rapidly under all conditions. As *We* increases, La/D_0 slowly increases at $15 < t^* < 20$ but suddenly decreases at $We = 73.4$ and 146.8. The lateral deformation widths of the downstream columns with different *We* values exhibit a peak of the transverse deformation at $t^* = 15$, after which it slowly decreases.

4.3. Modified material line stretching law and energy budget analysis

The change in the perimeter of the water column provides an intuitive indication of its degree of deformation. We defined the water mass fraction of 0.5 as the material interface and analyzed the dimensionless change in length of the interface over time. Furthermore, the material line growth rate was extracted, based on which we fitted a material line change model for a certain range of *We* values ($We < 100$). Thus, we devised a modified exponential stretching law model.

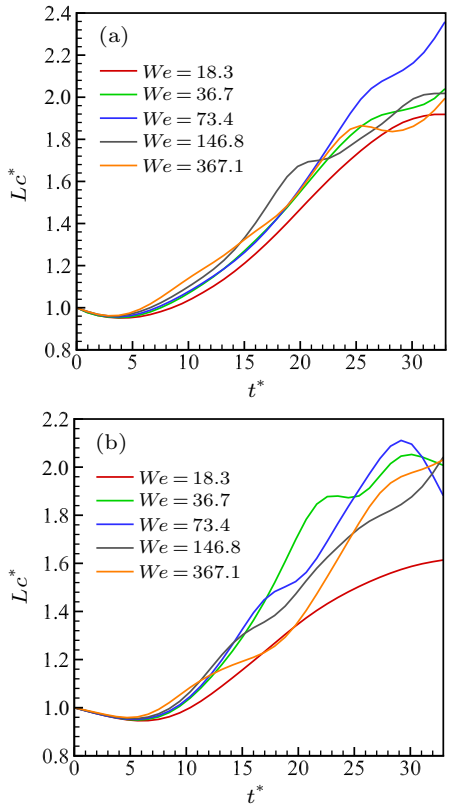


Fig. 17. Time variations of the normalized material line Lc^* for different *We* values: (a) the upstream column and (b) the downstream column. $Lc^* = Lc/Lc_0$.

Figure 17 shows the time variation of the normalized perimeter for two water columns for different *We* values. The

perimeter is also known as the material line. The material line is used as a mixing characteristic parameter of the material line length Lc (also known as the interfacial length). The water volume fraction contour $\alpha_l = 0.5$ was used to calculate $Lc^*(t^*)$ and is normalized by their initial values $Lc_0(t^* = 0)$. Previously, Yang *et al.*[39] found that the growth of $Lc^*(t^*)$ follows the exponential stretching law $Lc^*(t^*) = A\,e^{\lambda t^*}$, where A and λ ($\lambda = (1/L)(dL/dt)$) are the compression factor and the specific stretching rate exponent, respectively. The original exponential stretching model assumes that the stretching rate of the material line (λ) is a constant that does not vary with time, and that both λ and the compression factor A needs to be changed for different We numbers. However, based on our simulation results, we find that λ is not a constant. So we decided to revise the original model and construct a revised model that does not require modification of the model parameters according to Weber number changes in the range of Weber numbers we studied in order to obtain a more accurate stretching law for the material line.

On this basis, the growth rate λ of the material line for different diameters of upstream water columns was obtained (Fig. 18). Evidently, λ gradually increases with time when $t^* < 15$ and reaches the peak value at approximately $t^* = 17$; then, it decreases and maintains an oscillatory behavior. The value of λ does not change significantly when t^* is within the range of 10–15, which corresponds to the stage wherein the material line is consistent with the exponential stretching law.

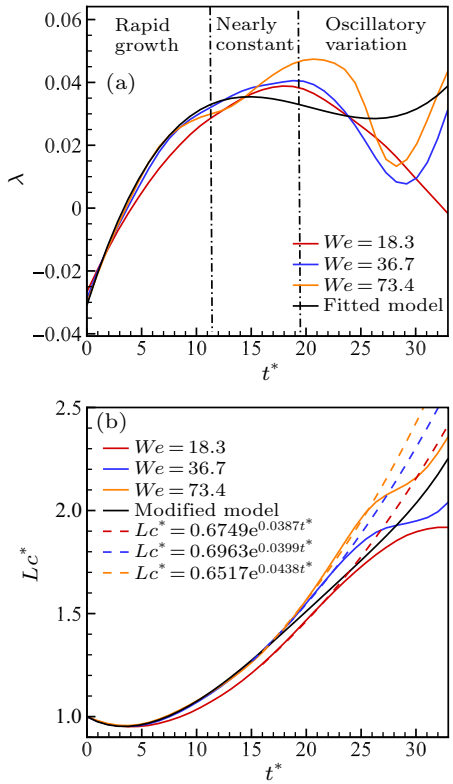


Fig. 18. Time variations of (a) material line growth rate and (b) normalized material line length Lc^* of upstream column. In panel (b), the solid lines denote numerical simulation results, and the dotted lines represent the exponential stretching law lines.

Furthermore, we extracted λ as a function of time and fitted the model with a cubic curve. We then compared the fitting results with the simulation results and exponential stretching model and found that the modified model of the upstream water column conforms better to the simulation results. Compared to the exponential stretching model, which exhibits an evident deviation in the initial stage, the modified model agrees well with the material line. It also conforms well to the rapid growth period of the material line. In the later stage, owing to the accuracy of the model, there is a certain degree of deviation; however, it still roughly reflects the change tendency of the material line for a wide We range. The original model can only describe the rapid stretching stage of the material line for a short time, while our modified model can accurately describe the stretching law of the material line in both the early stage of liquid column deformation and the rapid stretching stage when $We < 100$ and $t^* < 20$. It means that during the period of deformation for water cylinder, under the coupling of surface waves and inertial forces, there is a clear regularity in the liquid column material line stretching with time, and it is applicable in the small Weber number range. However, when the liquid column starts to break up, and the liquid film and liquid filaments start to pull out from the edge of the liquid column under the shear effect of airflow, these liquid bands will have cyclic fracture, which also leads to the failure of the original exponential stretching law. Considering that the present modified model is only a simple modified model, we still need to consider the Weber number effect when adjusting the model parameters in the higher Weber number cases ($We > 300$).

We counted the area of the liquid column at different moments and multiplied the area by the density to get the kinetic energy ($E_k = \int \frac{1}{2}\rho u^2 dS$). The water volume fraction contour $\alpha_l \geq 0.5$ was used to determine the mesh counts into the area. We also counted the perimeter of the column at different moments and multiplied the perimeter by the surface tension coefficient to get the surface energy ($E_\sigma = \sigma L_c$). The water volume fraction contour $\alpha_l = 0.5$ was used to calculate Lc. The energy is in the liquid column per unit height. As shown in Figs. 19(a) and 19(b), depicting the time variation of the energy of the upstream column, indicate good similarity and consistency. The kinetic energy is proportional to the square of We, and the surface tension energy is proportional to We. For the downstream column, figures 19(c) and 19(d) depict the time variation of the energy of the downstream column. It can be divided into two parts: when $t^* < 17$, the kinetic energy is proportional to the square of We, and when $t^* > 17$, the kinetic energy fluctuates randomly. The max value of E_k/We^2 first increases then decreases. The E_σ/We values show evident similarity when $t^* < 15$ and thereafter deviate.

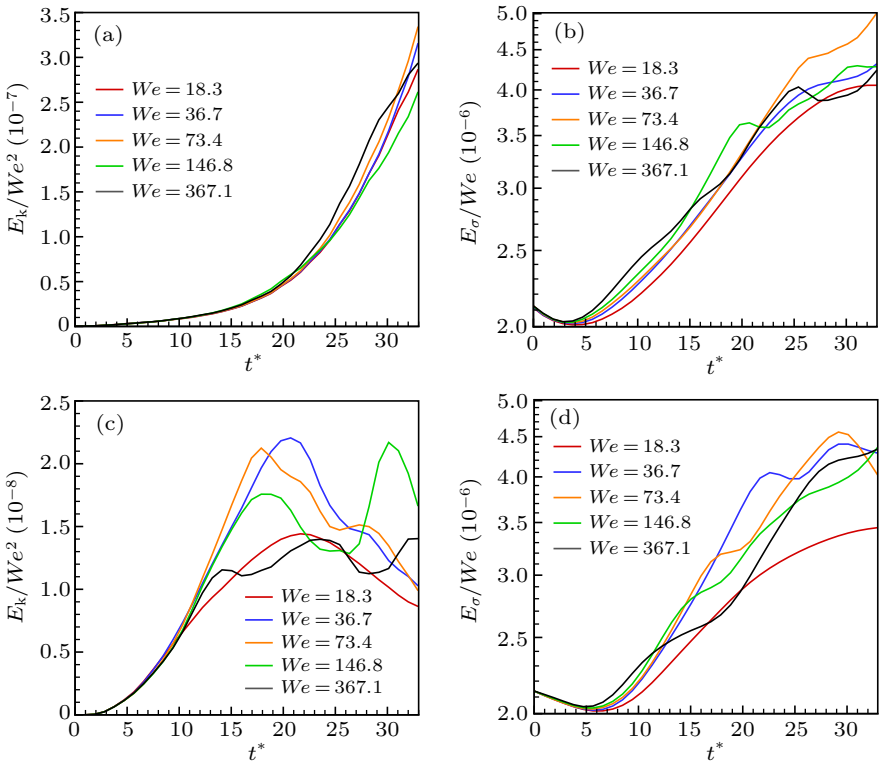


Fig. 19. Time variations of kinetic energy and surface energy for different *We* values. Panels (a) and (b) represent the upstream column, and panels (c) and (d) represent the downstream column.

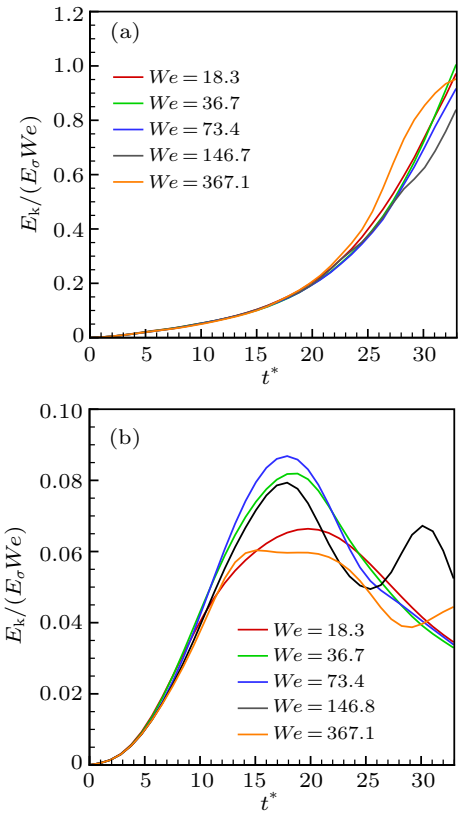


Fig. 20. Time variations of ratio of E_k and E_σ at different *We* values: (a) the upstream column and (b) downstream column.

Figure 20 shows the time variations of the ratio of kinetic energy and surface energy of the two columns. The ratio of the kinetic energy to the surface energy for the upstream water column evidently increases, and this ratio for the downstream water column attains a maximum value at approximately $t^* = 17$, after which it fluctuates. When $We = 18.4$, the maximum value of the aforementioned ratio for the upstream water column is 18, and the maximum value of the ratio for the downstream water column is 1.2. This result indicates the key role of the surface energy of the downstream water column in maintaining the shape of the column and thus prevent breakup. When $We = 36.7$, the maximum value of the ratio of the kinetic surface energy size of the upstream column is 40, and the maximum value of the ratio of the kinetic surface energy size of the downstream column is 3.2. The rapid increase in the kinetic energy of the column following the increase in *We* is the main reason for the water column breakup. The ratio of kinetic energy to the surface energy varies exponentially with *We* for the upstream column. Meanwhile, for the downstream column, the energy ratio causes the exponential trend to become oscillatory.

5. Conclusion

This study entailed a numerical investigation of the complex interplay between shock waves and interfaces. The aerobreakup of two consecutive water columns subjected to shock waves spanning a broad spectrum of Weber numbers was thoroughly examined.

As regards the morphology, as the Weber number increases, the upstream water–column breakup morphologies transition from flattening to bag breakup mode. Simultaneously, the downstream water column flattens on the windward

side, bends on the leeward side, and progressively forms a bag structure with increasing Weber number. The kinematic parameters and the degree of distortion observed in the two water columns reveal notable differences from the isolated one, while considerable similarities are apparent in the two columns at different Weber numbers. Specifically, the kinematic characteristics of the upstream column, including the velocity, displacement, and acceleration, exhibit consistent similarities across various Weber numbers. In contrast, the downstream column demonstrates satisfactory agreement in the initial stages, and it manifests a non-uniform oscillatory pattern in the later stage. Meanwhile, the interaction between the columns results in substantially smaller velocity and displacement values for the downstream column compared to the upstream column.

Subsequently, the temporal trends and relative magnitudes of kinetic energy and surface energy were examined from an energy perspective. Evidently, the kinetic energy of the upstream water column shows rapid growth under varying Weber numbers. In contrast, the kinetic energy of the downstream water column initially increases and reaches its peak before gradually decreasing. With regard to the surface energy, after an initial phase of nearly exponential growth, it demonstrates a slower growth phase. The surface energy dynamics of the downstream column are more intricate, illustrating similarities with the upstream column in the initial stages. However, the surface energy then exhibits a decrease, followed by a resurgence of growth after a period of rapid exponential increase.

The stretching rate of a material line is not uniform and undergoes variations over time. This variation exhibits a mild curvature with respect to time across a broad spectrum of Weber numbers. Furthermore, we present an improvement upon the initial exponential stretching law model of the material line to achieve a better alignment with the simulation results over a prolonged duration. The proposed model is more accurate over a wide range of Weber numbers.

The results of the existing work can serve for the physical modeling of droplet cluster interactions with shock waves, and thus go on to construct the fragmentation model as well as the drag model in the multi-droplet state. In future, it is necessary to improve the modified model by incorporating the influence of the Weber number. Moreover, the effects of the spacing between water columns must be investigated in order to gain further insight into the interaction dynamics between the front and back of the water columns and to elucidate the breakup mode for various spacing conditions.

Data availability statement

The data that support the findings of this study are available from the corresponding author upon reasonable request.

Acknowledgements

Project supported by the National Natural Science Foundation of China (Grant Nos. 12202070 and 11772065) and the Foundation of National Key Laboratory of Computational Physics.

References

[1] Theofanous T G 2011 *Annu. Rev. Fluid Mech.* **43** 661
[2] Harper E Y, Grube G W and Chang I D 1972 *J. Fluid Mech.* **52** 565
[3] Hinze J O 1955 *AIChE J.* **1** 289
[4] Pilch M and Erdman C A 1987 *Int. J. Multiph. Flow* **13** 741
[5] Guildenbecher D R, López-Rivera C and Sojka P E 2009 *Exp. Fluids* **46** 371
[6] Sembian S, Liverts M, Tillmark N and Apazidis N 2016 *Phys. Fluids* **28** 056102
[7] Meng J C and Colonius T 2018 *J. Fluid Mech.* **835** 1108
[8] Liu N, Wang Z, Sun M, Wang H and Wang B 2018 *Acta Astronautica* **145** 116
[9] Dorschner B, Biasiori-Poulanges L, Schmidmayer K, El-Rabii H and Colonius T 2020 *J. Fluid Mech.* **904** A20
[10] Lin J Y, Shen Y, Ding H, Liu N S and Lu X Y 2017 *J. Comput. Phys.* **328** 140
[11] Wang B, Xiang G and Hu X Y 2018 *Int. J. Multiph. Flow* **104** 20
[12] Xiang G and Wang B 2017 *J. Fluid Mech.* **825** 825
[13] Xu S, Fan W, Wu W, Wen H and Wang B 2023 *J. Fluid Mech.* **964** A12
[14] Nicholls J A and Ranger A A 1969 *AIAA J.* **7** 285
[15] Liu Z and Reitz R D 1997 *Int. J. Multiph. Flow* **23** 631
[16] Theofanous T G and Li G J 2008 *Phys. Fluids* **20** 052103
[17] Liu D Y, Anders K and Frohn A 1988 *Int. J. Multiph. Flow* **14** 217
[18] Mulholland J A, Srivastava R K and Wendt J O L 1988 *AIAA J.* **26** 1231
[19] Nguyen Q V and Dunn-Rankin D 1992 *Exp. Fluids* **12** 157
[20] Holländer W and Zaripov S K 2005 *Int. J. Multiph. Flow* **31** 53
[21] Temkin S and Ecker G Z 1989 *J. Fluid Mech.* **202** 467
[22] Igra D and Takayama K 2003 *J. Fluids Eng.* **125** 325
[23] Kim I, Elghobashi S and Sirignano W 1991 29*th Aerospace Sciences Meeting Reno*, NV, USA, 1991-01-07
[24] Kim I, Elghobashi S and Sirignano W 1992 30*th Aerospace Sciences Meeting and Exhibit Reno*, NV, USA, 1992-01-06
[25] Kim I, Elghobashi S and Sirignano W A 1993 *J. Fluid Mech.* **246** 465
[26] Prahl L, Revstedt J and Fuchs L 2006 44*th AIAA Aerospace Sciences Meeting and Exhibit Reno*, Nevada, 2006-01-09
[27] Shao C, Luo K and Fan J 2017 *Chem. Eng. J.* **308** 619
[28] Stefanitsis D, Malgarinos I, Strotos G, Nikolopoulos N, Kakaras E and Gavaises M 2019 *Int. J. Multiph. Flow* **113** 289
[29] Magi V and Abraham J 2012 Launceston, Australia, 2012-12-03
[30] Kapila A K, Menikoff R, Bdzil J B and Son S F 2001 *Phys. Fluids* **13** 3002
[31] Richard Saurel, Petitpas F and Berry R A 2009 *J. Comput. Phys.* **228** 1678
[32] Schmidmayer K, Petitpas F, Daniel E, Favrie N and Gavrilyuk S 2017 *J. Comput. Phys.* **334** 468
[33] Le Métayer O, Massoni J and Saurel R 2005 *J. Comput. Phys.* **205** 567
[34] Kaiser J W J, Winter J M, Adami S and Adams N A 2020 *Int. J. Multiph. Flow* **132** 103409
[35] Van Leer B 1977 *J. Comput. Phys.* **23** 263
[36] Shyue K M and Xiao F 2014 *J. Comput. Phys.* **268** 326
[37] Schmidmayer K, Petitpas F and Daniel E 2019 *J. Comput. Phys.* **388** 252
[38] Schmidmayer K, Petitpas F, Le Martelot S and Daniel É 2020 *Comput. Phys. Commun.* **251** 107093
[39] Yang J, Kubota T and Zukoski E E 1993 *AIAA J.* **31** 854